# Electronic Supplementary Information

## Elevating the p-band centre of $SnO_2$ nanosheets through W incorporation for promoted $CO_2$ electroreduction

Dong Fang,[a] Linlin Zhang,*[a, b] Yongjian Niu,[a] Yuanyuan Wang,[a] Qingxiao Su,[a] Jiao Wang,[a] and Cheng Wang*[a]

[a] Institute for New Energy Materials and Low-Carbon Technologies

School of Material Science and Engineering

Tianjin Key Laboratory of Advanced Functional Porous Materials

Tianjin University of Technology

Tianjin 300384, People's Republic of China

[b] CAS Key Laboratory of Design and Assembly of Functional Nanostructures

Fujian Key Laboratory of Nanomaterials

Fujian Institute of Research on the Structure of Matter, Chinese Academy of Sciences

Fuzhou 350002, People's Republic of China

* Corresponing author: Linlin Zhang, zhanglinlin_cn@126.com;

Cheng Wang, cwang@tjut.edu.cn

## Table of contents

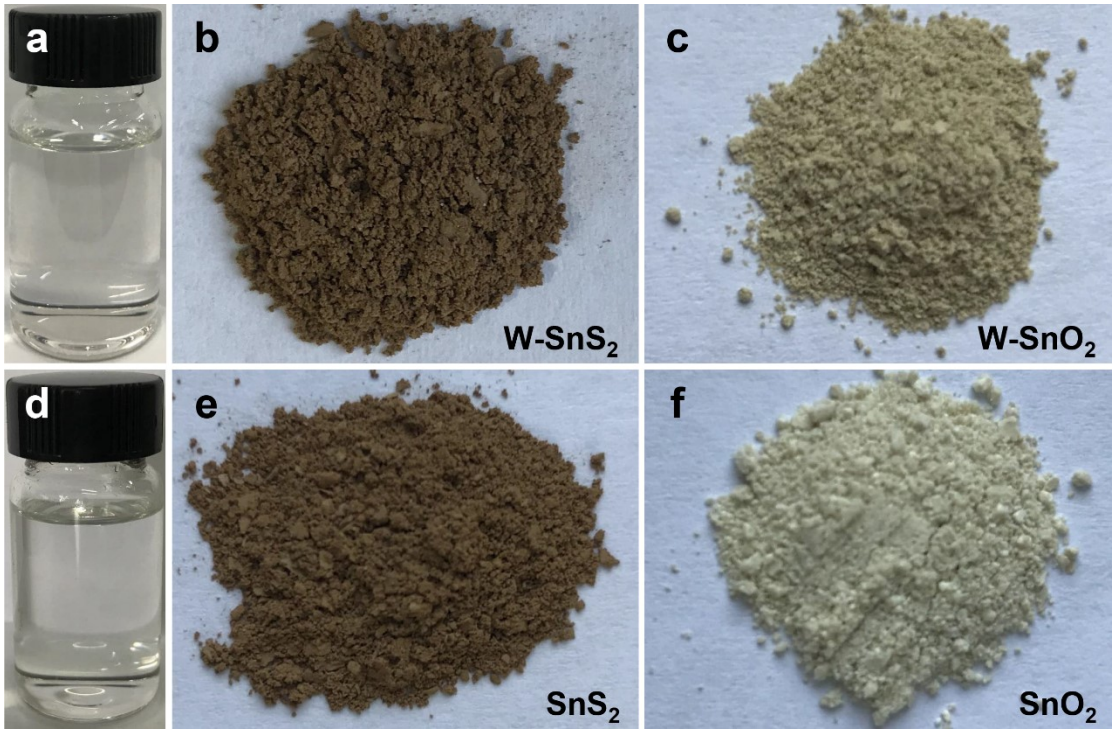


**Fig. S1** Photographs of the precursor solutions prior to solvothermal treatment (a, d), the precursors after solvothermal treatment (b, e) and the products after calcination in air (c, f) for W-$SnO_2$ (a-c) and $SnO_2$ (d-f).

**Table S1**. Detailed synthetic conditions for the control samples

| Entry | Sample | Solvothermal | | | | | | Air-calcination | |
|---|---|---|---|---|---|---|---|---|---|
| | | n($SnCl_2·2H_2O$) (mmol) | n($WCl_6$) (mmol) | n(L-cys[a]) (mmol) | Temp. (°C) | Time (h) | Solvent | Time (h) | Rate (°C $min^{-1}$) |
| 1 | $SnS_2$ | 1.00 | 0 | 2.4 | 180 | 6 | NMP | - | - |
| 2 | $SnS_2$-1 | 1.00[b] | 0 | 2.4 | 180 | 6 | NMP | - | - |
| 3 | $SnS_2$-2 | 1.00[c] | 0 | 2.4 | 180 | 6 | NMP | - | - |
| 4 | $SnS_2$-oil[d] | 1.00 | 0 | 2.4 | 180 | 6 | NMP | - | - |
| 5 | W-$SnS_2$ | 0.98 | 0.02 | 2.4 | 180 | 6 | NMP | - | - |
| 6 | 1%W-$SnS_2$ | 0.99 | 0.01 | 2.4 | 180 | 6 | NMP | - | - |
| 7 | 5%W-$SnS_2$ | 0.95 | 0.05 | 2.4 | 180 | 6 | NMP | - | - |
| 8 | 8%W-$SnS_2$ | 0.92 | 0.08 | 2.4 | 180 | 6 | NMP | - | - |
| 9 | W-$SnS_2$-100 | 0.98 | 0.02 | 2.4 | 100 | 6 | NMP | - | - |
| 10 | W-$SnS_2$-200 | 0.98 | 0.02 | 2.4 | 200 | 6 | NMP | - | - |
| 11 | W-$SnS_2$-3h | 0.98 | 0.02 | 2.4 | 100 | 3 | NMP | - | - |
| 12 | W-$SnS_2$-9h | 0.98 | 0.02 | 2.4 | 100 | 9 | NMP | - | - |
| 13 | W-$SnS_2$-0 | 0.98 | 0.02 | 0 | 180 | 6 | NMP | - | - |
| 14 | W-$SnS_2$-1.2 | 0.98 | 0.02 | 1.2 | 180 | 6 | NMP | - | - |
| 15 | W-$SnS_2$-3.6 | 0.98 | 0.02 | 3.6 | 180 | 6 | NMP | - | - |
| 16 | W-$SnS_2$-iPrOH | 0.98 | 0.02 | 3.6 | 180 | 6 | iPrOH | - | - |
| 17 | W-$SnS_2$-EtOH | 0.98 | 0.02 | 3.6 | 180 | 6 | EtOH | - | - |
| 18 | W-$SnS_2$-MeOH | 0.98 | 0.02 | 3.6 | 180 | 6 | MeOH | - | - |
| 19 | W-$SnS_2$-EG | 0.98 | 0.02 | 3.6 | 180 | 6 | EG | - | - |
| 20 | W-$SnS_2$-$H_2O$ | 0.98 | 0.02 | 3.6 | 180 | 6 | $H_2O$ | - | - |
| 21 | W-$SnS_2$-DMF | 0.98 | 0.02 | 3.6 | 180 | 6 | DMF | - | - |
| 22 | $SnO_2$ | 1.00 | 0 | 2.4 | 180 | 6 | 500 | 2 | 2 |
| 23 | W-$SnO_2$ | 0.98 | 0.02 | 2.4 | 180 | 6 | 500 | 2 | 2 |
| 24 | 1%W-$SnO_2$ | 0.99 | 0.01 | 2.4 | 180 | 6 | 500 | 2 | 2 |
| 25 | 1%W-$SnO_2$ | 0.99 | 0.01 | 2.4 | 180 | 6 | 500 | 2 | 2 |
| 26 | 1%W-$SnO_2$ | 0.99 | 0.01 | 2.4 | 180 | 6 | 500 | 2 | 2 |

[a] L-cys was short for L-cysteine.

[a] $K_2SnO_3·3H_2O$ was used as the Sn source instead of $SnCl_2·2H_2O$ for the synthesis of the typical sample of $SnS_2$.

[b] $SnCl_4$ was used as the Sn source instead of $SnCl_2·2H_2O$ for the synthesis of the typical sample of $SnS_2$.

[c] An oil bath approach was used instead of the solvothermal method for the synthesis of the typical sample of $SnS_2$.

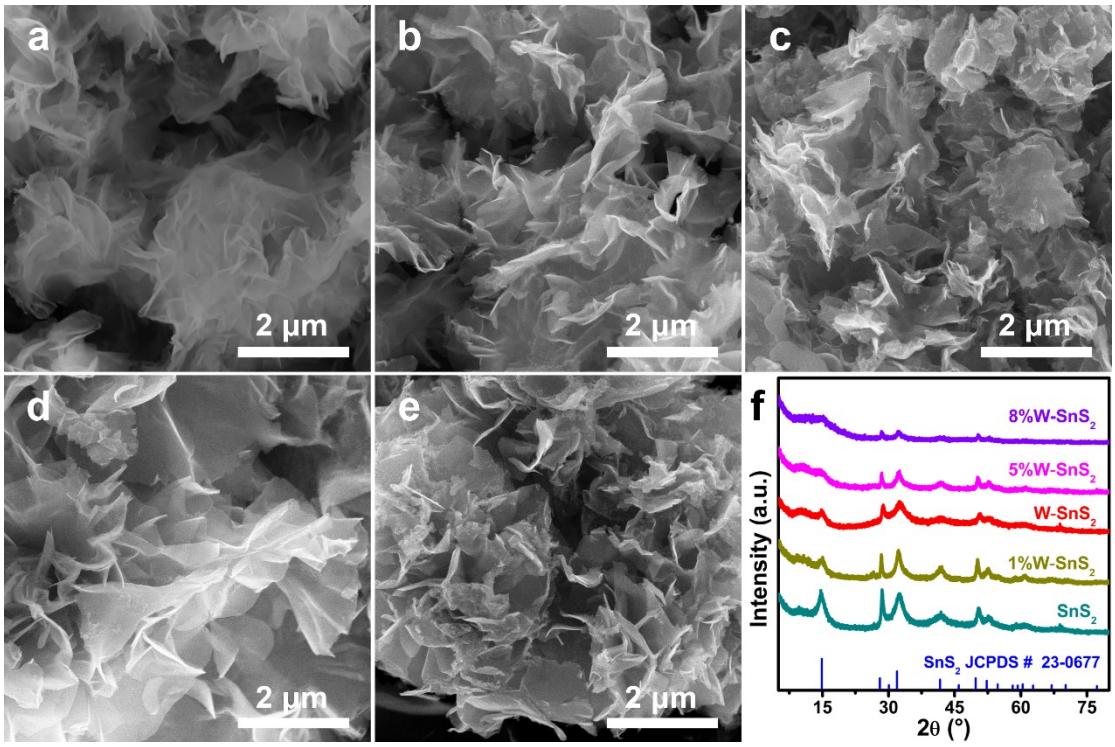


**Fig. S2** SEM images of $SnS_2$ (a), 1%W-$SnS_2$ (b), W-$SnS_2$ (c), 5%W-$SnS_2$ (d), 8%W-$SnS_2$ (e) and the corresponding XRD patterns (f).

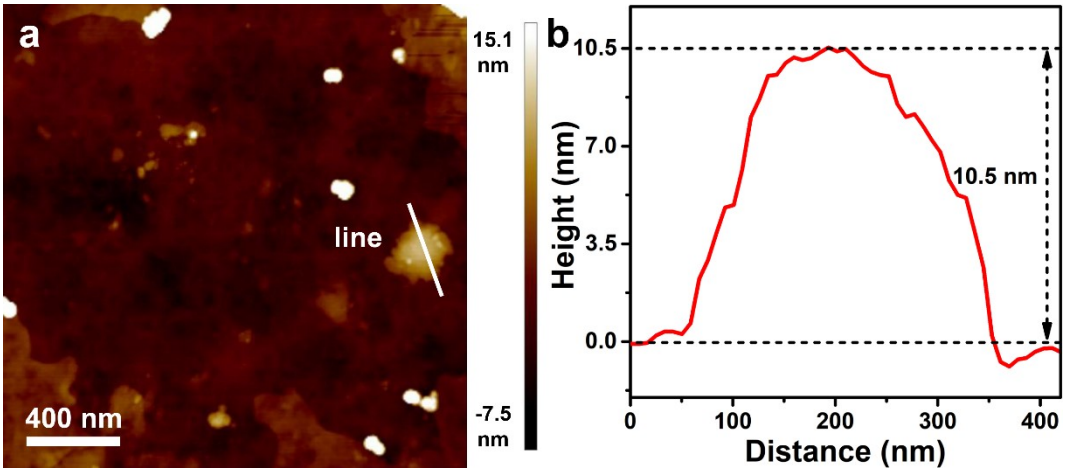


**Fig. S7** AFM image (a) and the corresponding height profile (b) for the sample of W-$SnO_2$.

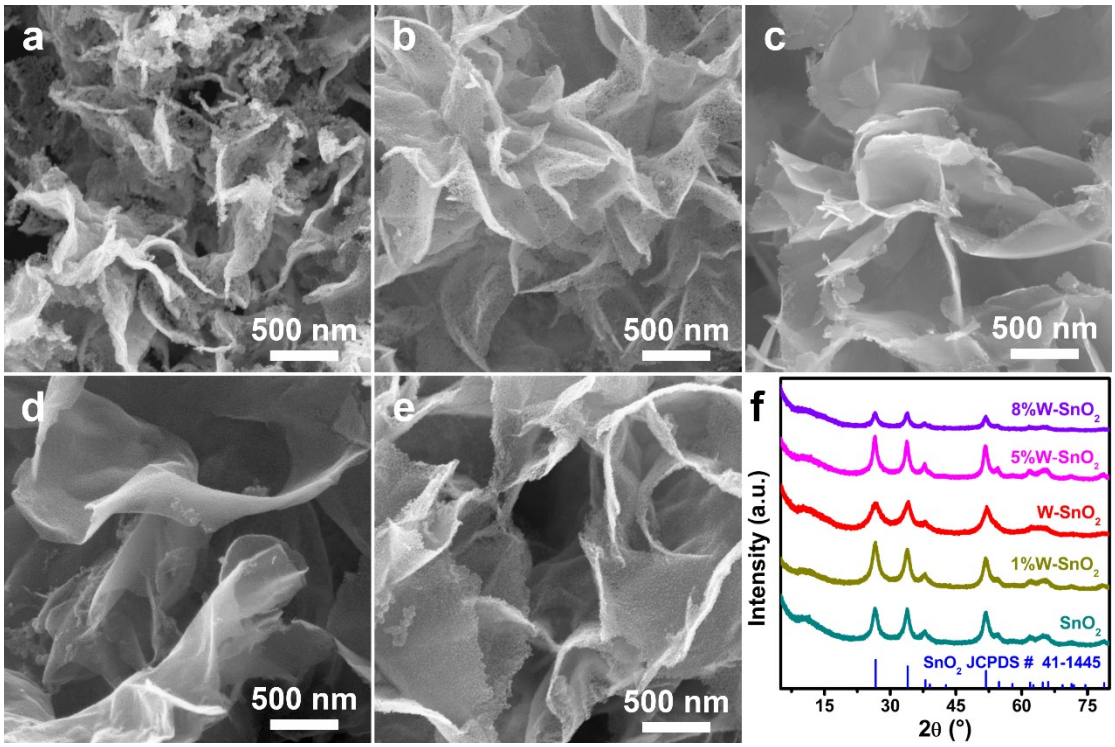


**Fig. S3** SEM images of $SnO_2$ (a), 1%W-$SnO_2$ (b), W-$SnO_2$ (c), 5%W-$SnO_2$ (d), 8%W-$SnO_2$ (e) and the corresponding XRD patterns (f).

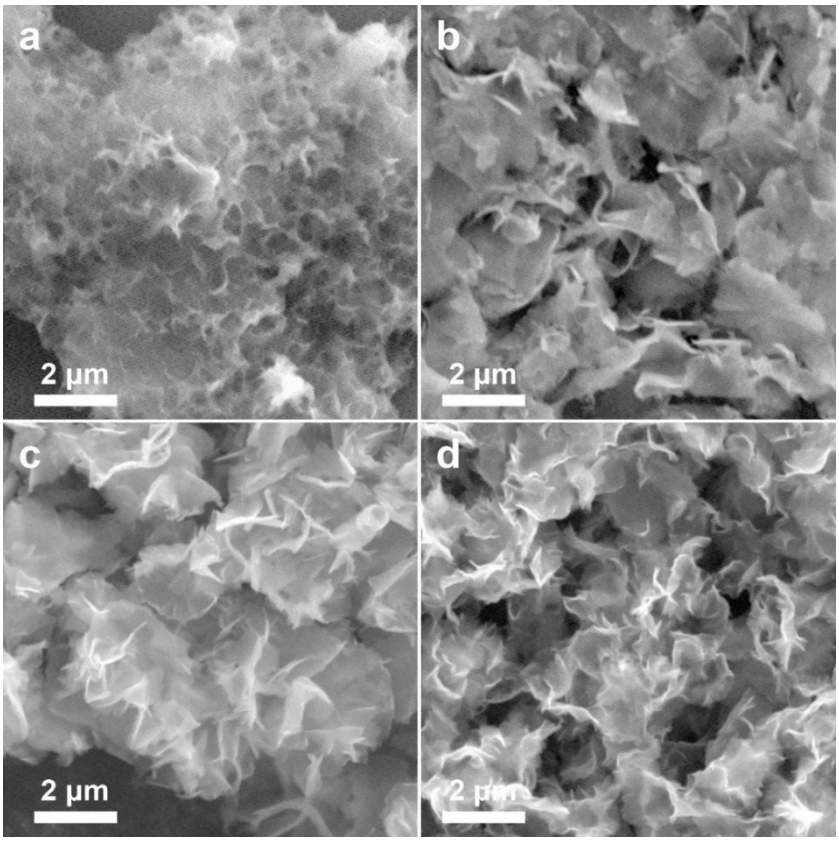


**Fig. S4**. SEM images for samples prepared by changing the reaction temperature (a-b) and time (c-d) during the solvothermal process under otherwise identical conditions for the typical sample of SnS2. (a) 100 $^{o}$C, (b) 200 $^{o}$C, (c) 3 h, (d) 9 h.

At lower temperatures (e. g., 100 $^{o}$C), tiny flurry nanosheets were assembled into aggregates, while at higher temperatures (e.g., 200 $^{o}$C), the sheets grew bigger and became more dispersed (**Fig. S4 a-b**). By and large, sheet-like morphologies were remained at different temperatures. On the other hand, as the reaction time extended from 3 to 9 h, the morphologies of the samples showed no obvious change (**Fig. S4 c-d**). This indicates that the nanosheets can be formed at an early stage of the reaction.

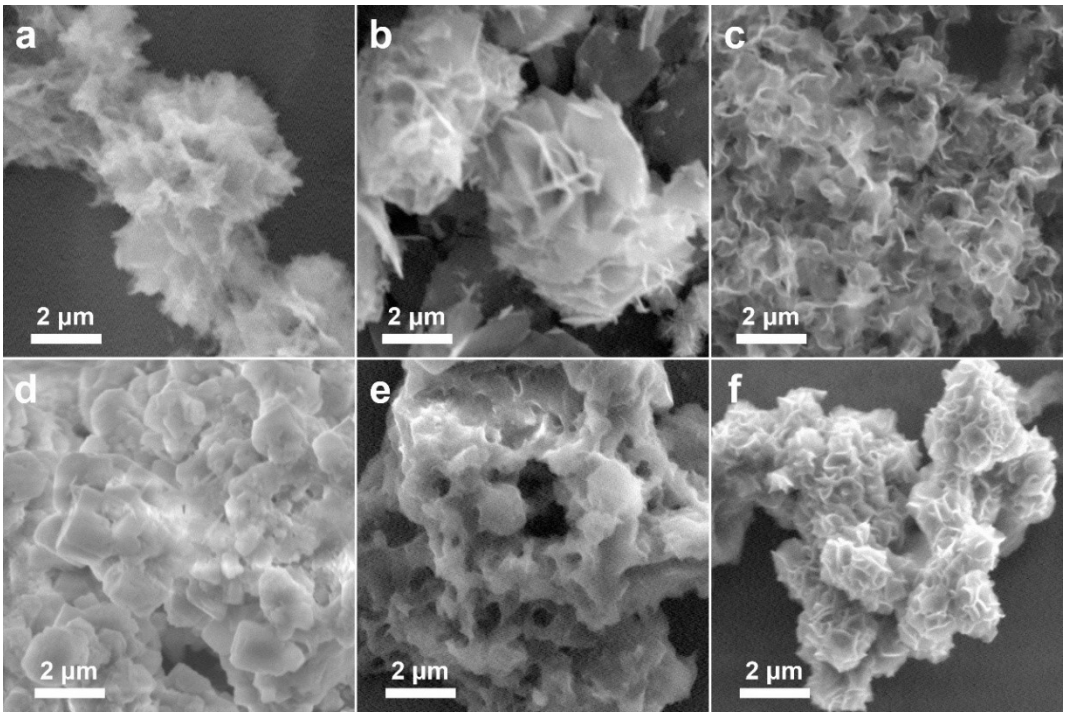


**Fig. S5**. SEM images for samples prepared by varying the dosage of L-cysteine (a-c) and Sn source (d-e) during the solvothermal process, and by using an oil-bath approach (f) under otherwise identical conditions for the typical sample of $SnS_2$. (a) 0 mmol, (b) 1.2 mmol, (c) 3.6 mmol, (d) $K_2SnO_3{\cdot}H_2O$, (e) $SnCl_4$, (f) oil bath.

Interestingly, without the S source, i. e., L-cysteine, the products also exhibited flurry sheet-like nanostructures. With less L-cysteine (1.2 mmol), thicker nanosheets were formed along with regular ones. With more L-cysteine (3.6 mmol), the nanosheets became thinner, curly, and loosely packed (**Fig. S5 a-c**). Obviously, L-cysteine exerted no significant influences on the formation of nanosheets, but did impact the state and dimensional size of the nanosheets. Noticeably, when the Sn source was changed from $SnCl_2{\cdot}2H_2O$ to $K_2SnO_3{\cdot}H_2O$ or $SnCl_4$, dramatical changes were observed. In both cases, only large irregular blocks could be found (**Fig. S5 d-e**). Unambiguously, the Sn source, particularly, the valence state of Sn, played crucial roles in the formation of nanosheets of tin sulfides. When an oil-bath approach was used instead of the solvothermal method under otherwise identical conditions, the products also manifested sheet-like morphologies. The only difference lied in that they were more rigid and compact than the typical sample (**Fig. S5 f**). It seemed that the in situ generated high pressure during the solvothermal process was not the key factor governing the morphology of the products.

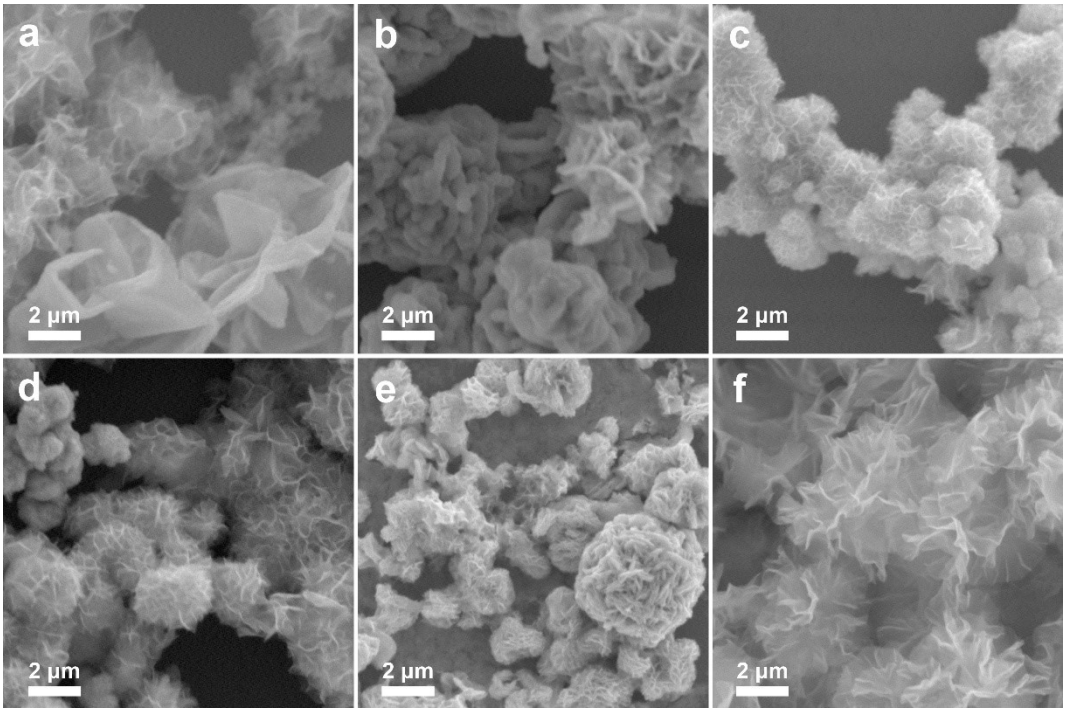


**Fig. S6**. SEM images for samples prepared in different solvents under otherwise identical synthetic conditions for the typical sample of $SnS_2$. (a) iPrOH, (b) EtOH, (c) MeOH, (d) ethylene glycol (EG), (e) $H_2O$ and (f) DMF.

Different solvents including iPrOH, EtOH, MeOH, ethylene glycol (EG), $H_2O$ and DMF were used to replace NMP in the solvothermal process. As can be seen from the SEM images (**Fig. S6 a-f**), inhomogeneous products were obtained in the polar protic solvents. Particularly, in iPrOH, EtOH or $H_2O$, aggregates of thicker nanosheets were observed accompanied by regular ones. For the cases utilizing MeOH or EG as the solvents, thin and rigid nanosheets were assembled into flower-like or irregular nanostructures. It's noteworthy that in DMF, thin nanosheets were obtained, which were analogous to the samples obtained in NMP. This might be due to the polar aprotic nature and the presence of Lewis base functional groups in these two solvents. Overall, the products exhibited sheet-like nanostructures in all the investigated solvents. However, only the polar aprotic solvents bearing amine functional groups were beneficial for the growth of thin and homogeneous nanosheets. The polar aprotic nature enables a good dissolution of reactants in the solvents, thus allowing for a homogeneous nucleation process of the products. On the other hand, the amide or mine groups are supposed to adsorb on the specific facets of $SnS_2$, for instance, the (001) facets. In this way, the growth of the products would be inhibited along the [001] direction with the evolution of crystallization process. This finally resulted in the formation of sheet-like nanostructures exposed with the (001) facets.

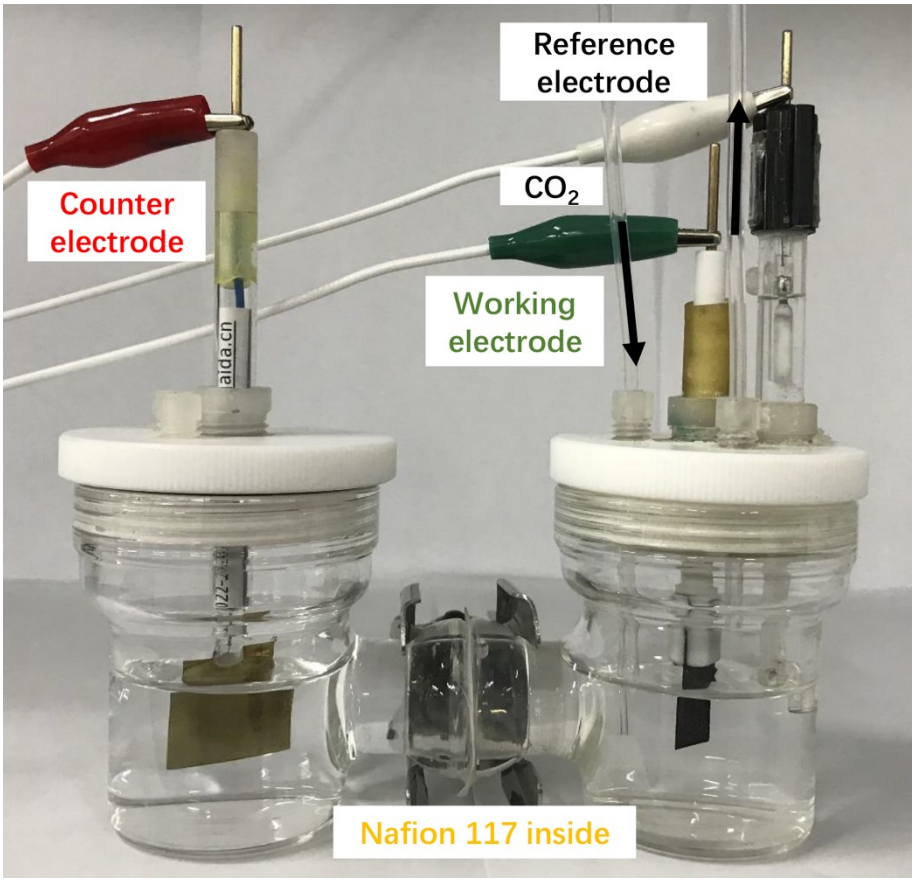


**Fig. S8** Photograph of the reactor for $CO_2$RR.

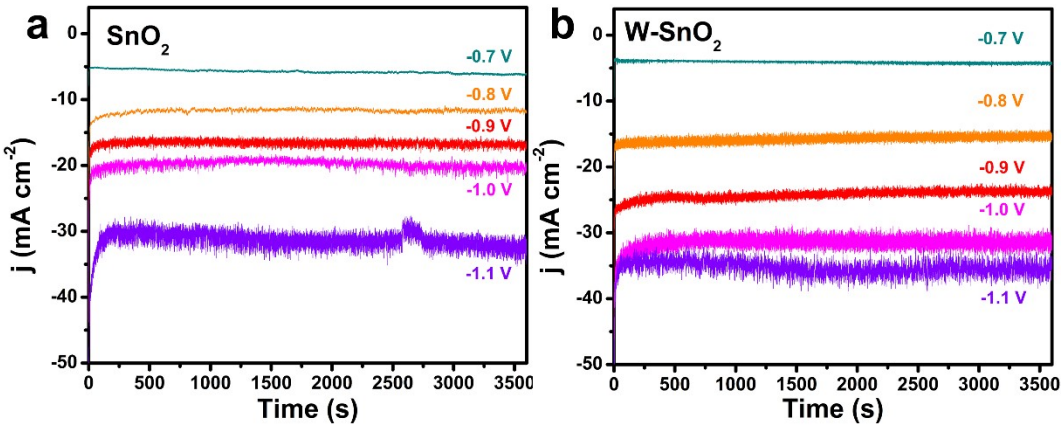


**Fig. S9** Chronoamperometric responses at different potentials during the electrolysis for 1 h for $SnO_2$ and W-$SnO_2$.

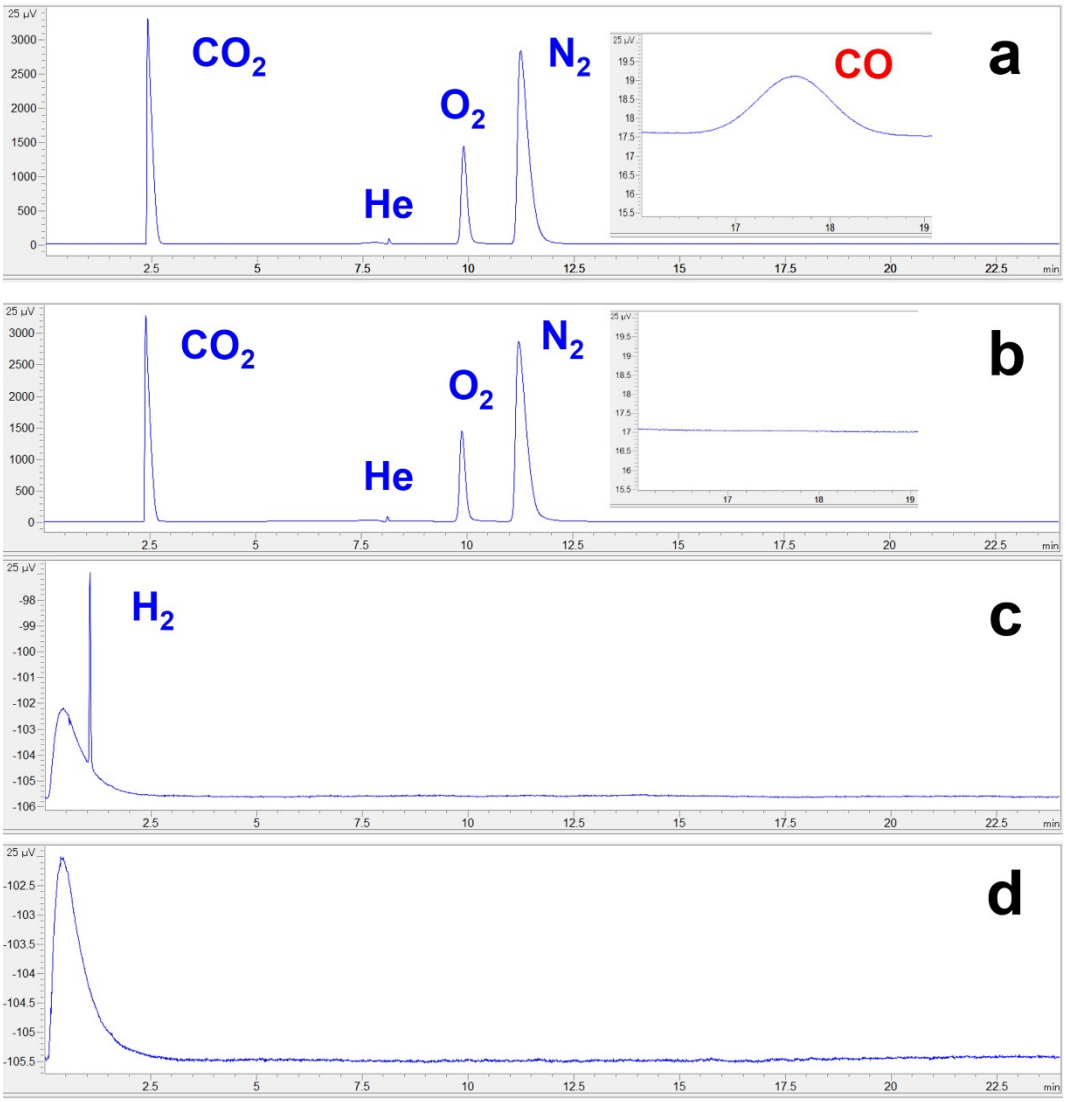


**Fig. S10** GC results detected by FID (a-b) and TCD (c-d) for W-$SnO_2$ in $CO_2$-saturated 0.5 M $KHCO_3$ aqueous solutions after electrolysis at -0.9 V for 1 h (a and c) and for pure $CO_2$ gas directly purged into GC (b and d). The peaks at about 2.1-2.2 min in c and d might be due to the mechanical disturbance during the GC valve shift.

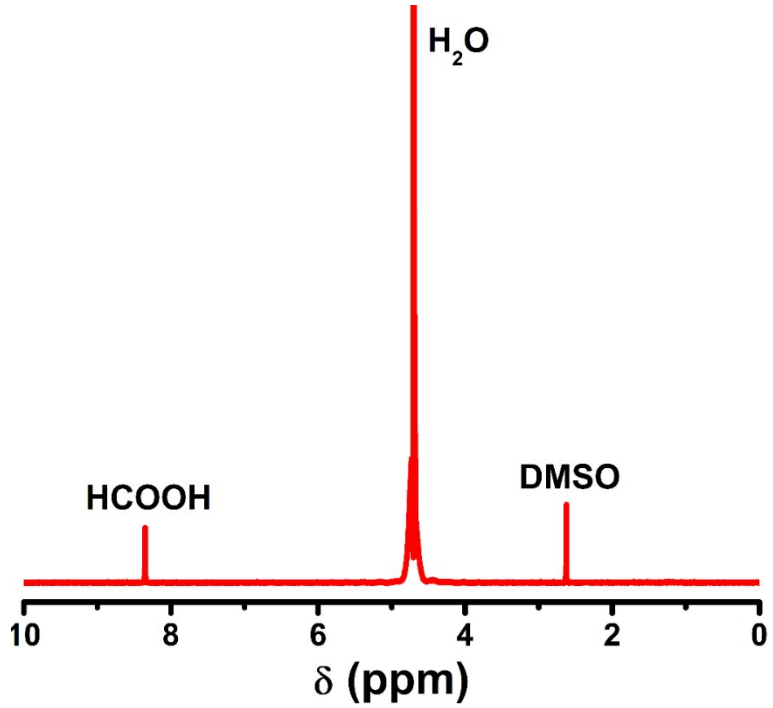


**Fig. S11** $^{1}$H-NMR spectra of the electrolyte after electrolysis at -0.9 V for 1 h with W-$SnO_2$ as the catalyst. The peak occurring at the chemical shift of 8.33 ppm was inactive of the formation of HCOOH.

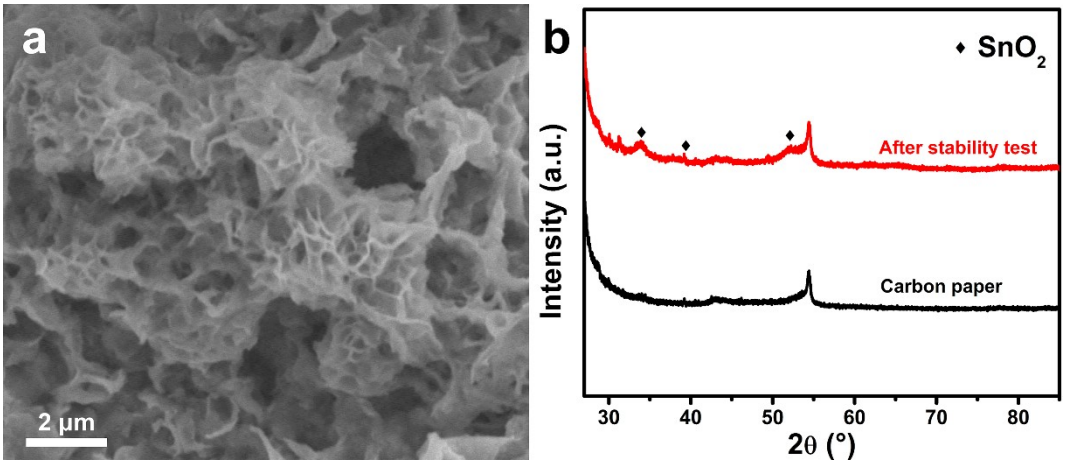


**Fig. S12** SEM image and XRD patterns for W-$SnO_2$ after the stability test, namely, electrolysis at -0.9 V for 14 h.

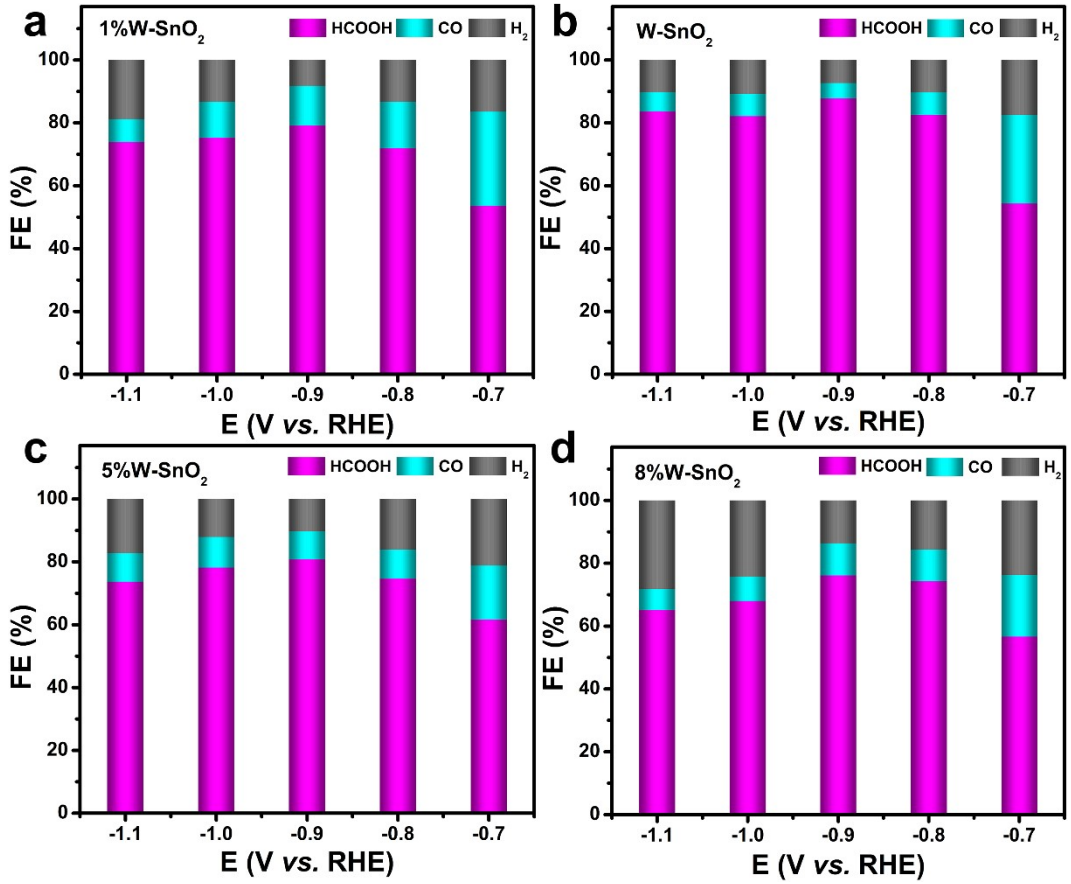


**Fig. S13** Potential-dependent faradaic efficiencies of HCOOH, CO and $H_2$ for $SnO_2$ nanosheets with different doping concentrations of W. (a) 1%W-$SnO_2$, (b) W-$SnO_2$ (2%W-SnO2), (c) 5%W-$SnO_2$, (d) 8%W-$SnO_2$.

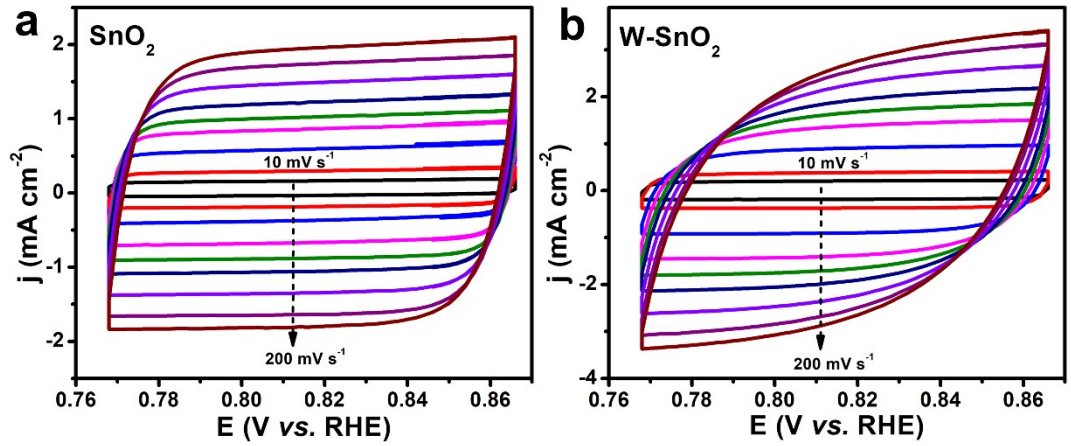


**Fig. S14** Scan rate-dependent CV curves for $SnO_2$ (a) and W-$SnO_2$ (b) at the non-faradaic potential regions.

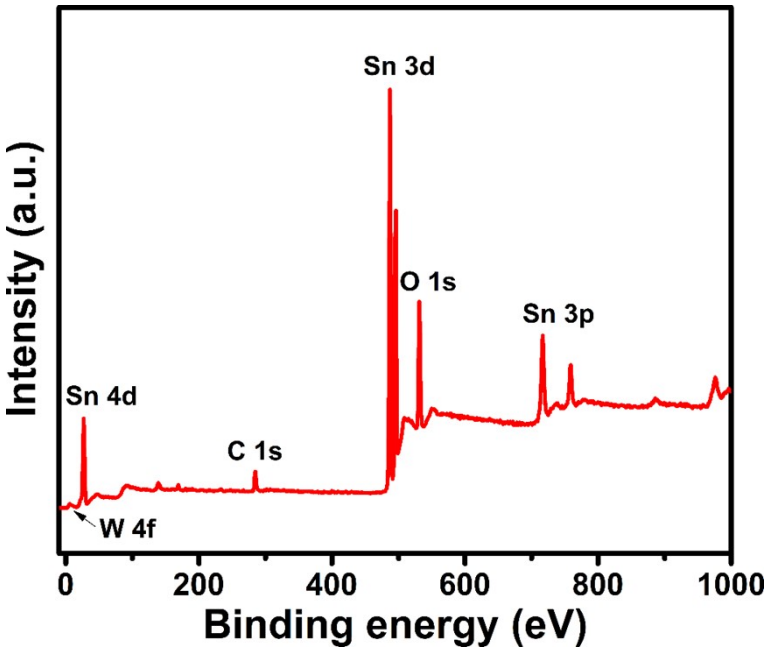


**Fig. S15** The survey XPS for the sample of W-$SnO_2$.

**Table S2**. Detailed information of the survey XPS for W-$SnO_2$.

| Name | Start BE (eV) | Peak BE (eV) | End BE (eV) | Height | Peak area | Atomic ratio |
|---|---|---|---|---|---|---|
| O1s | 544.9 | 531.13 | 525.1 | 73123.52 | 157961.18 | 0.178205 |
| W4f | 47.9 | 28.2 | 28.1 | 792.3 | 1257.58 | 0.001419 |
| Sn3d | 499.9 | 487.19 | 479.1 | 245264.69 | 727180.67 | 0.820376 |

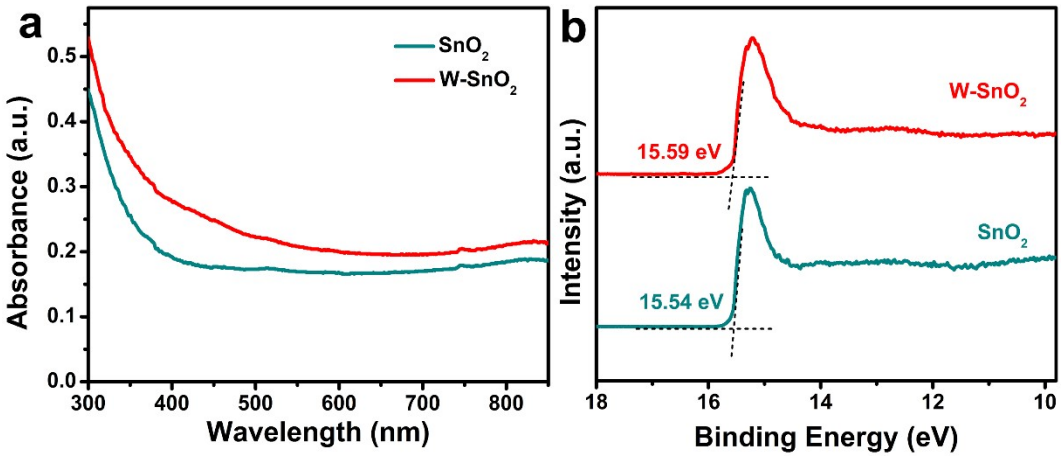


**Fig. S16** UV-vis diffuse reflectance spectra (a) and the secondary electron cutoff edge of UPS (b) for the samples of $SnO_2$ and W-$SnO_2$.

**Table S3**. Performance comparison with reported Sn-based catalysts for $CO_2$ electroreduction to HCOOH

| Catalyst | Electrolyte | Potential (V vs. RHE) | $FE_{HCOOH}$ (%) | Current density (mA $cm^{-2}$) | Reference |
|---|---|---|---|---|---|
| W-$SnO_2$ | 0.5 M $KHCO_3$ | -0.90 | 87.8 | 20.9 | This work |
| $SnS_2$/rGO | 0.5 M $NaHCO_3$ | -0.75 | 84.5 | 13.9 | [1] |
| Sn/$SnO_2$ | 0.1 M $KHCO_3$ | -0.90 | 82.1 | 27.9 | [2] |
| $Bi_{52}Sn_{46}In_2$ | 0.1 M $KHCO_3$ | -1.20 | 82.0 | 30.5 | [3] |
| mp-$SnO_2$ | 0.1 M $KHCO_3$ | -1.15 | 75.0 | 14.4 | [4] |
| WIT $SnO_2$ | 0.1 M $KHCO_3$ | -0.99 | 69.0 | 12.0 | [5] |
| Sn-pNWs | 0.1 M $NaHCO_3$ | -1.00 | 79.0 | 10.0 | [6] |
| Sn dendrite | 0.1 M $KHCO_3$ | -1.06 | 59.0 | 11.0 | [7] |
| Sn/SnOx | 0.5 M $NaHCO_3$ | -0.70 | 40.0 | 4.0 | [8] |
| Sn/CF | 0.5 M $KHCO_3$ | -0.80 | 65.0 | 11.0 | [9] |
| $V_o$-$SnO_2$ | 0.5 M $KHCO_3$ | -1.10 | 68.4 | 44.2 | [10] |
| $SnO_2$ | 0.5 M NaOH | -0.60 | 67.6 | 3.5 | [11] |
| $SnO_2$-Sn | 0.5 M $KHCO_3$ | -0.80 | 73.0 | 10.0 | [12] |
| Pd/$SnO_2$ NSs | 0.1 M $NaHCO_3$ | -0.24 | 54.0 | 1.4 | [13] |
| $SnO_2$/Py-CNTO | 0.1 M $KHCO_3$ | -1.29 | 85.0 | 29.8 | [14] |
| $Sn_3O_4$ | 0.5 M $KHCO_3$ | -0.90 | 85.1 | 16.2 | [15] |
| $SnO_2$ NPs | 0.1 M $KHCO_3$ | -1.10 | 85.0 | 23.7 | [16] |
| $Zn_2SnO_4$/$SnO_2$ | 0.1 M $KHCO_3$ | -1.08 | 77.0 | 5.8 | [17] |
| $Cu_3Sn$/$Cu_6Sn_5$ | 0.1 M $NaHCO_3$ | -1.00 | 82.0 | 20.0 | [18] |
| $SnO_2$ NWs | 0.1 M $KHCO_3$ | -1.16 | 87.0 | 13.7 | [19] |
| AgSn/$SnO_x$ | 0.5 M $NaHCO_3$ | -0.80 | 80.0 | 16.0 | [20] |

## References


[1] F. Li, L. Chen, M. Xue, T. Williams, Y. Zhang, D. R. MacFarlane and J. Zhang, *Nano Energy*, 2017, **31**, 270-277.

[2] H. Hu, L. Gui, W. Zhou, J. Sun, J. Xu, Q. Wang, B. He and L. Zhao, *Electrochim. Acta*, 2018, **285**, 70-77.

[3] F.-M. Allioux, S. Merhebi, M. B. Ghasemian, J. Tang, A. Merenda, R. Abbasi, M. Mayyas, T. Daeneke, A. P. O'Mullane, R. Daiyan, R. Amal and K. Kalantar-Zadeh, *Nano Lett.*, 2020, **20**, 4403-4409.

[4] R. Daiyan, X. Lu, W. H. Saputera, Y. H. Ng and R. Amal, *ACS Sustainable Chem. Eng.*, 2018, **6**, 1670-1679.

[5] L. Fan, Z. Xia, M. Xu, Y. Lu and Z. Li, *Adv Funct. Mater.*, 2018, **28**, 1706289.

[6] B. Kumar, V. Atla, J. P. Brian, S. Kumari, T. Q. Nguyen, M. Sunkara and J. M. Spurgeon, *Angew. Chem. Int. Ed.*, 2017, **56**, 3645-3649.

[7] D. H. Won, C. H. Choi, J. Chung, M. W. Chung, E.-H. Kim and S. I. Woo, *ChemSusChem*, 2015, **8**, 3092-3098.

[8] Y. Chen and M. W. Kanan, *J. Am. Chem. Soc.*, 2012, **134**, 1986-1989.

[9] Y. Zhao, J. Liang, C. Wang, J. Ma and G. G. Wallace, *Adv. Energy Mater.*, 2018, **8**, 1702524.

[10] H. He, K. Liu, K. Liang, A. Mustapha, Z. Wang, L. Wu, C. Yang, L. Deng, S. Guo and Y.-N. Liu, *J. Catal.*, 2020, **385**, 246-254.

[11] S. Lee, J. D. Ocon, Y.-i. Son and J. Lee, *J. Phys. Chem. C*, 2015, **119**, 4884-4890.

[12] R. Ma, Y.-L. Chen, Y. Shen, H. Wang, W. Zhang, S.-S. Pang, J. Huang, Y. Han and Y. Zhao, *RSC Adv.*, 2020, **10**, 22828-22835.

[13] W. Zhang, Q. Qin, L. Dai, R. Qin, X. Zhao, X. Chen, D. Ou, J. Chen, T. T. Chuong, B. Wu and N. Zheng, *Angew. Chem. Int. Ed.*, 2018, **57**, 9475-9479.

[14] Y. Zhang, H. Xu, D. Niu, X. Zhang and Y. Zhang, *ChemSusChem*, 2021, **14**, 2769-2779.

[15] Z. Chen, M.-R. Gao, N. Duan, J. Zhang, Y.-Q. Zhang, T. Fan, J. Zhang, Y. Dong, J. Li, Q. Liu, X. Yi and J.-L. Luo, *Appl. Catal. B: Environ.*, 2020, **277**, 119252.

[16] R. Daiyan, E. C. Lovell, N. M. Bedford, W. H. Saputera, K.-H. Wu, S. Lim, J. Horlyck, Y. H. Ng, X. Lu and R. Amal, *Adv. Sci.*, 2019, **6**, 1900678.

[17] K. Wang, D. Liu, P. Deng, L. Liu, S. Lu, Z. Sun, Y. Ma, Y. Wang, M. Li, B. Y. Xia, C. Xiao and S. Ding, *Nano Energy*, 2019, **64**, 103954.

[18] J. Wang, J. Zou, X. Hu, S. Ning, X. Wang, X. Kang and S. Chen, *J. Mater. Chem. A*, 2019, **7**, 27514-27521.

[19] S. Liu, J. Xiao, X. F. Lu, J. Wang, X. Wang and X. W. Lou, *Angew. Chem. Int. Ed.*, 2019, **58**, 8499-8503.

[20] W. Luc, C. Collins, S. Wang, H. Xin, K. He, Y. Kang and F. Jiao, *J. Am. Chem. Soc.*, 2017, **139**, 1885-1893.